# Analysis of the heat transfer and anti-corrosion performance of an aluminum nitride porous ceramic skeleton with controllable preparation

Huan Wang[a,b], Ziyuan Li[a], Zhen Shang[a*], Limei Tian[a*], Shuai Zhang[c], Yuying Yan[c]

[a]Key Laboratory of Bionic Engineering, Ministry of Education, Jilin University, Changchun, 130022, P. R. China.

[b]School of Engineering, Shenyang Agricultural University, Shenyang, 110866, P. R. China.

[c]Faculty of Engineering, University of Nottingham, Nottingham, NG7 2RD, UK.

*Corresponding authors, E-mail: shangzhen@jlu.edu.cn & lmtian@jlu.edu.cn

## Abstract

Porous skeletons play a positive role in improving the heat storage and release rate of molten salt phase change materials, making their development a research hot spot. However, the current simple structure of the porous skeletons limits their application in complex heat storage devices. In this study, the aluminum nitride porous ceramic skeleton, prepared by the photocuring additive manufacturing technology, was shown to improve the heat transfer performance of a solar salt. The solar salt/aluminum nitride porous ceramic skeleton composite phase change materials were prepared and their heat storage rate was investigated. The composite phase change materials could reduce the heat storage time by up to 33.05 % compared to the pure solar salt; the maximum temperature difference decreased by up to 22.1 ℃. Even after 180 heat cycles, the aluminum nitride porous ceramic skeletons exhibited excellent anti-corrosion against the solar salt and maintained their original phase, functional groups, and elements, with no new compound formation. This study is of great significance to improve the heat

storage performance of complex heat storage devices and provides a foundation for the application of ceramic additive manufacturing in the field of energy storage and heat transfer.

**Keywords:** Porous ceramic; photocuring additive manufacturing; solar salt; heat transfer; anti-corrosion

| Nomenclature | | $Al_2O_3$ | Aluminum oxide |
|---|---|---|---|
| AlN | Aluminum nitride | $NaNO_3$ | Sodium nitrate |
| PCMs | Phase change materials | $KNO_3$ | Potassium nitrate |
| SiC | Silicon carbide | LSI | Liquid silicon infiltration |
| LCD | Liquid crystal display | XRD | *X*-ray diffraction |
| $Y_2O_3$ | Yttrium oxide | EDS | Energy dispersive spectroscopy |

## 1. Introduction

To alleviate the growing energy demands worldwide, various novel energy harvesting methods are being developed with improved energy conversion efficiencies. Common thermal energy storage technologies include electrochemical heat storage, sensible heat storage and phase change heat storage [1]. Compared to other methods, phase change heat storage exhibits the advantages of high energy storage density and low costs [2]. It has been applied in industrial waste heat recovery, solar energy storage, and staggered peak energy storage [3-6]. Based on their phase change temperature of the phase change materials (PCMs), they can be divided into low-temperature PCMs, medium-temperature PCMs, and high-temperature PCMs [7, 8]. In general, low-temperature PCMs are mainly organic [9-12], whereas, medium- and high-temperature

PCMs are inorganic [13-17].

Notably, the low thermal conductivity of PCMs reduces their heat storage and release rate, and therefore, improving the heat storage and release rate of PCMs has become a major research focus. PCMs heat storage and release rate have been enhanced using various methods, such as microcapsules [18, 19], metallic skeletons [20, 21], and metal fins [22, 23]. However, these methods are commonly applied only to low-temperature PCMs [24]. Medium- and high-temperature PCMs generally exhibit strong corrosive [25, 26], which makes it difficult to apply to the abovementioned heat-transfer enhancement methods. In addition, several studies have tried adding nanoparticles to enhance the PCMs properties [27-29]. However, phase separation often occurs between the nanoparticles and PCMs after repeated heat storage and release cycles, making the two incompatible [30].

Porous skeletons also play an important role in heat storage and release rate [31, 32], which are commonly prepared using metallic, carbon-based, and ceramic materials [33-35]. Ceramic materials exhibit excellent (i) anti-corrosion properties compared to metals and (ii) mechanical performance compared to carbon-based materials. Owing to these properties, the incorporation of porous ceramic skeletons in PCMs has demonstrated improved heat storage and release rate [36-38]. Luo et al. [39] prepared three-dimensional (3D) hierarchical ultralight silicon carbide (SiC) foams, obtained from nickel (Ni) foam by annealing, chemical vapor deposition, and gas phase infiltration. Compared to pure PCMs, the thermal conductivity increased by 259% for the composites. Li et al. [40] studied the effective thermal conductivity of $NaLiCO_3$-

based composites, prepared by combining magnesium oxide (MgO; i.e. the ceramic skeleton), PCMs, and heat transfer enhancers. Xu et al. [41] prepared biomorphic SiC foams with high thermal conductivity (up to 116 W/mK) by reactive infiltration of molten silicon (Si) into carbonized wood. Zhang et al. [42] prepared SiC porous ceramic materials by impregnating polyurethane foam with a SiC slurry and studied the molten salt/SiC composite PCMs. They showed that the porous SiC can reduce the maximum temperature difference of the molten salt phase change from 148 ℃ to 130 ℃ and increase the heat storage rate by 42.9%.

From the above studies, it is clear that porous ceramics play a crucial role in improving the heat transfer rate of molten salt PCMs. However, the heat storage device structures are generally complicated and the shape of the porous ceramic is not controllable. Thus, poorly matched shapes increase the thermal resistance and reduce the heat storage rate. Therefore, the preparation of porous ceramic materials with controllable structures has become an important goal of energy storage research. With the continuous development of additive manufacturing, the porous ceramic skeletons of the additive manufacturing have found extensive applications in the field of heat transfer [43-45]. However, their effect on improving PCMs heat storage rate remains unclear.

In this study, the heat transfer properties of solar salt/AlN porous ceramic skeleton composite PCMs were analyzed. Four AlN porous ceramic skeletons, with porosities in the range of 60.46–82.20%, were prepared by using a liquid crystal display (LCD) 3D printer. Further, the anti-corrosion property of the AlN porous ceramic skeleton in the

solar salt composite PCMs was investigated. We aimed to improve the rate of heat storage devices with complex structures and provide a foundation for the application of 3D-printed porous ceramic materials in heat storage applications.

## 2. Methods and meethods

### 2.1 Materials

The photosensitive resin (transparent) was procured from Shenzhen Creality 3D Technology Co., Ltd., China; AlN ceramic powder with two different diameters (6.5 μm and 3 μm; purity≥99.9%) from Hebei Keze Metal Materials Co., Ltd., China; yttrium oxide ($Y_2O_3$) and aluminum oxide ($Al_2O_3$) powders (purity≥99.5%, average particle diameter of 1 μm) from Hubei Nona Technology Co., Ltd., China; silica fume (purity ≥ 99.5%, average particle size of 6 μm) from Qinghe Chuangying Metal Material Co., Ltd., China; and sodium nitrate ($NaNO_3$) and potassium nitrate ($KNO_3$) (purity≥99.9%) from Shanghai Aladdin Industrial Inc., China. The photosensitive resin was used as the raw material for the LCD 3D printer; $Y_2O_3$ and $Al_2O_3$ were used as sintering aids, and the silica fume was used for the liquid silicon infiltration (LSI) materials. The solar salt was prepared using a mixture of $NaNO_3$ and $KNO_3$.

### 2.2 AlN porous ceramic skeleton preparation

Four different models of the AlN porous ceramic skeleton were established in the 3D modeling software (detailed structural dimensions and nomenclature of the porous skeleton have been listed (Table 1)). The overall dimensions of the porous models were 70 mm × 59 mm × 55 mm. Subsequently, the 3D geometric porous model was sliced using the CHITUBOX 64 software into 0.05 mm thick layers, and the curing time of

each layer was 20 s [35]. The sliced porous skeleton model was then imported into the LCD 3D printer [LD-002H; Fig. 1(b)], and the mixed AlN ceramic slurry was introduced into the material tank of the printer [Fig. 1(a)]. The porous green body skeleton was then printed [Fig. 1(c)] and carbonized in a furnace (GF1750, Nanjing Boyuntong Instrument) under a nitrogen ($N_2$) atmosphere [Figs. 1(d, e)]. The carbonization process was as follows: the temperature was increased from 20-150 ℃ over 65 min; it was then increased to 500 ℃ over the next 700 min, and maintained at that temperature for 30 min; finally, natural cooling temperature ranges from 500 ℃ to room temperature. The carbonized porous skeleton was placed in a furnace for liquid silicon infiltration (LSI) under an argon (Ar) atmosphere [Figs. 1(f, g)]. The LSI process was as follows: The skeleton temperature was gradually increased from 25-600 ℃ over 115 min; 600-1100 ℃ over 50 min; and 1100-1550 ℃ over 150 min. The temperature was maintained at 1550 ℃ for 120 min. It was subsequently cooled down to 1100 ℃ over 100 min, and then, to room temperature naturally.

**Table 1.** Dimensions of the AlN porous skeleton structure.

| Name | Pore (mm) | Strut (mm) | Long (mm) | Wide (mm) | Height (mm) |
|---|---|---|---|---|---|
| I | 3.5 | 0.5 | | | |
| II | 2.5 | 0.5 | 70 | 59 | 55 |
| III | 3.5 | 0.8 | | | |
| IV | 2.5 | 0.8 | | | |

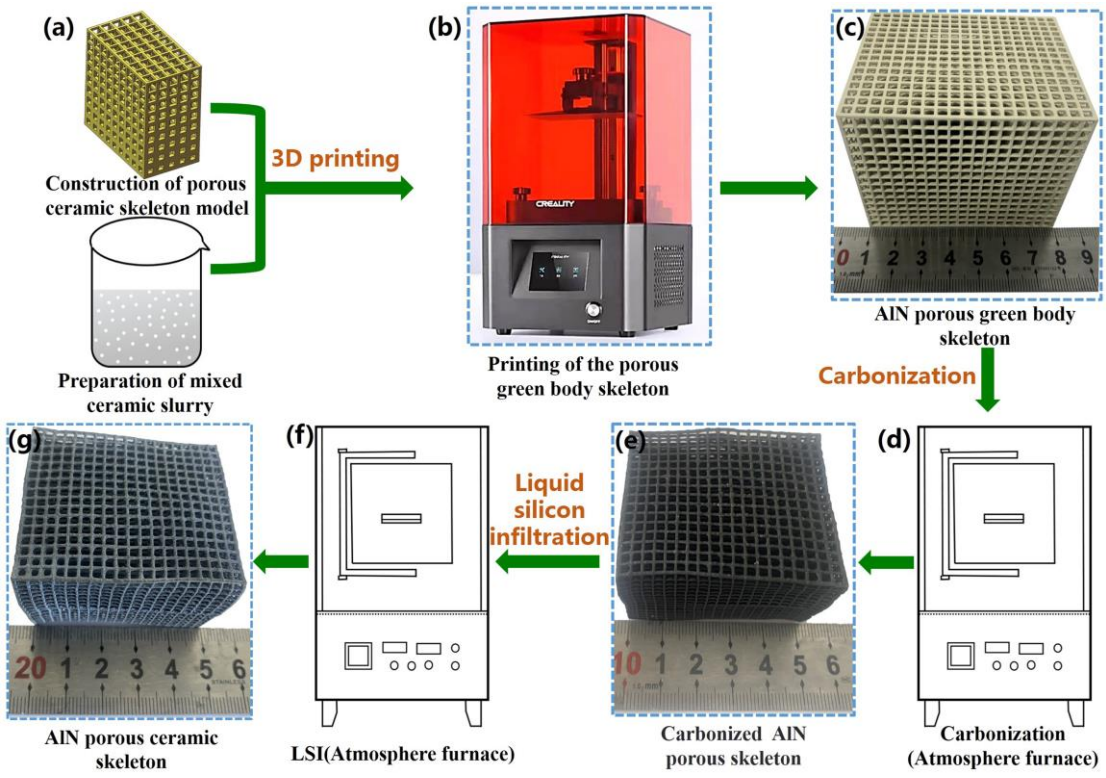


**Fig. 1.** AlN porous ceramic skeleton preparation process. (a) ceramic slurry and porous model, (b) LCD 3D printer, (c) the porous green body skeleton, (d) carbonization in the atmosphere furnace, (e) porous skeleton after carbonization, (f) LSI in the atmosphere furnace, and (g) ceramic skeleton after LSI.

## 2.3 Heat transfer experiment of the porous ceramic skeleton

Solar salts find extensive applications in solar thermal power plants, waste heat recovery, and other related fields [28]. They are classified as inorganic PCMs, which possess substantial latent heat and excellent thermal stability. In this study, a solar salt was employed as the PCMs (thermo-physical properties in Table 2). The heat source of the heat transfer test device was a 250 W aluminum (Al) heating plate of dimensions 100 mm × 100 mm × 20 mm [Fig. 2(a)]. During the heat transfer test, the temperature of the heating plate was set to 300 ℃ and regulated by the temperature controller. Previous studies have shown that ceramic surfaces exhibit excellent wettability [47, 48].

Therefore, the solar salt/AlN porous ceramic skeleton composite PCMs was contained in a transparent quartz cuboid box (56 mm × 36 mm × 56 mm) under atmospheric pressure. To reduce heat transfer from the surrounding environment, the quartz cuboid box was sealed using an insulating brick.

**Table 2.** Thermo-physical properties of the solar salt [42, 46].

| m($NaNO_3$): m($KNO_3$) | Density, kg/$m^3$ | Solidus temperature, ℃ | Liquidus temperature, ℃ | Thermal conductivity, W/m.K |
|---|---|---|---|---|
| 6:4 | 1980 | 225 | 246 | 0.59(solid) / 0.48(liquid) |

The composite PCMs temperature field was monitored during melting using three thermocouple temperature sensors (K type-RNK-191/E), fixed in the quartz cuboid box at three different points ($Q_1$, $Q_2$, and $Q_3$). $Q_1$ and $Q_3$ were located 20 mm away from the left and right walls of the quartz cuboid box and $Q_2$ was located at its center; all the sensors were placed 20 mm above the bottom of the quartz cuboid box. As the salt melted, the temperature change inside the quartz cuboid box was recorded by the sensors, and the data was collected once per minute using a connected temperature recorder. Additionally, the melting liquid fraction and temperature change of the composite PCMs were recorded every 10 min using a digital camera (Nikon-D7500) and a hand-held infrared thermometer (HIKVISION-HM-TPH16-6VF/W). Every experiment was repeated thrice.

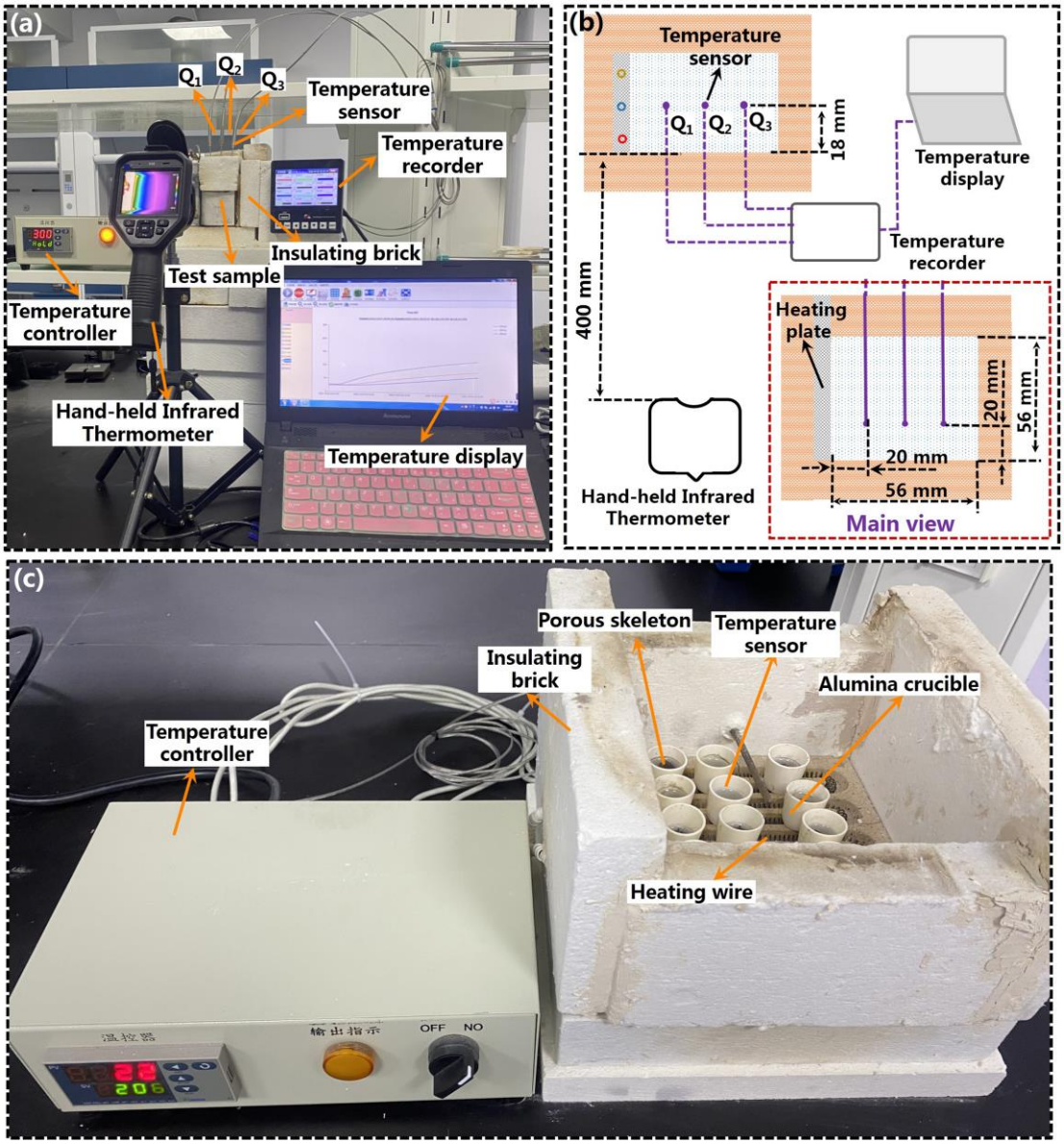


**Fig. 2.** Testing device. (a) Heat transfer testing device, (b) Schematic of the heat transfer testing device, and (c) corrosion testing device.

## 2.4 Thermal conductivity tests

The thermal conductivity of the solar salt/AlN porous ceramic skeleton composite PCMs was determined using a thermal conductivity tester (DRE-III, Xiangtan Xiangyi Instrument Co., Ltd., China), which is equipped with a hot disk probe and employs the transient plane source method. The ceramic skeleton was cut into two pieces of dimensions 50 mm × 50 mm × 10 mm.

Then, the molten solar salt was injected into the two skeletons, followed by a waiting period for the composite PCMs to cool down to room temperature. The probe of the thermal conductivity tester was securely clamped between the two solar salt/AlN porous ceramic skeleton composite PCMs and firmly affixed using a specialized clamping device, ensuring complete contact between the sample and the probe. The voltage of the thermal conductivity tester was set to 0 V using the test software and the thermal conductivity of the solar salt/AlN porous ceramic skeleton composite PCMs was estimated. Materials with similar thermal conductivities are presented in the reference table. Finally, the heating power, test time, and sampling interval were inputted into the testing parameter selection interface based on the material test values in the reference table, and obtained the thermal conductivities of the composite PCMs through testing. To eliminate the randomness of the experiment, each group of tests was repeated thrice and the mean thermal conductivity values were computed.

**2.5 Corrosion experiment**

To evaluate the anti-corrosion of the AlN porous ceramic skeleton, the AlN porous ceramic skeleton (with different porosities) and copper (Cu) metal foam (volume = 1$cm^3$) were separately mixed with the solar salt for heat cycle testing in an alumina crucible. A nickel (Ni)-chromium (Cr) alloy wire was used as the heat source, which could heat up to 850 ℃. The temperature sensors measured the temperature at a distance of 40 mm above the center of the experimental device heating wire. The top of the experimental device remained unsealed, resulting in rapid loss of a significant amount of heat energy. The quartz crucible was directly connected to the heating wire. The

temperature change of the heat cycles was controlled by the temperature controller [Fig. 2(b)]. The temperature controller was set as follows:

(i) Heating temperature is 80 ℃~245 ℃, and the heating time is 8 min;

(ii) Keep the temperature at 245 ℃ for 2 min;

(iii) Cooling temperature is 80 ℃~245 ℃, and the cooling time is 16 min;

(iv) Keep the temperature at 245 ℃ for 2 min;

(v) The heat cycles program repeats from (i).

The structural changes in the Cu foam and ceramic skeleton after 60, 120, and 180 heat cycles were recorded using the digital camera. Finally, the structure and composition of the ceramic skeleton, after the heat cycles, were analyzed by *X*-ray diffraction and Raman spectroscopy.

## 3. Results and discussion

### 3.1 Structural analysis

The ceramic slurry solid loading and sintering process parameters have been described in detail in the supplementary material. $P_I$ is the porous green body skeleton with pore size of 3.5 mm and strut size of 0.5 mm after LSI. $P_{II}$ is the porous green body skeleton with pore size of 2.5 mm and strut size of 0.5 mm after LSI. $P_{III}$ is the porous green body skeleton with pore size of 3.5 mm and strut size of 0.8 mm after LSI. $P_{IV}$ is the porous green body skeleton with pore size of 2.5 mm and strut size of 0.8 mm after LSI.

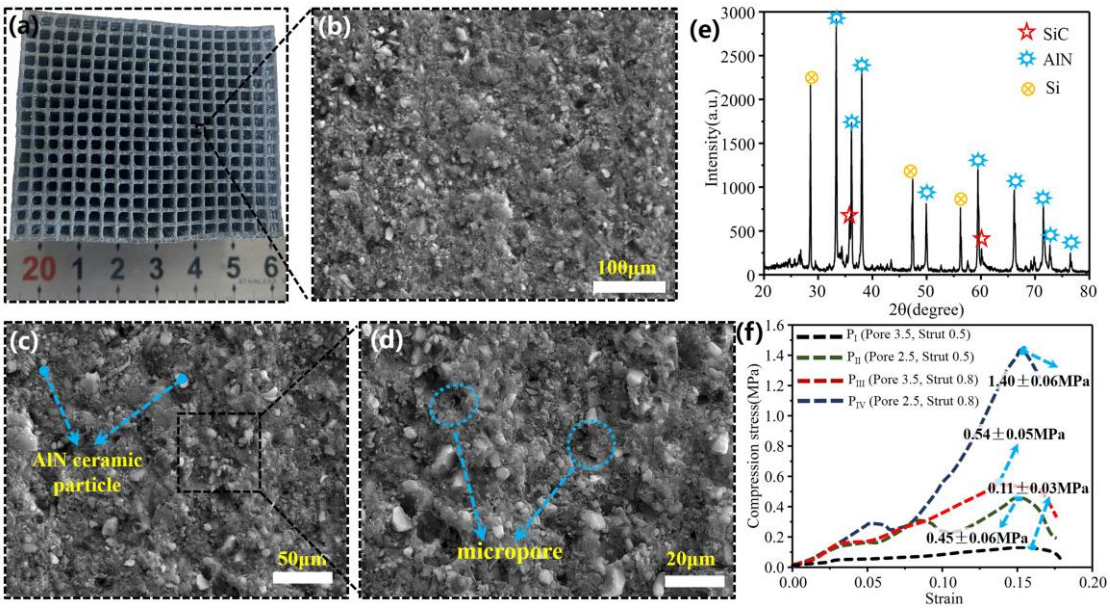


**Fig. 3.** (a) AlN porous ceramic skeleton; (b-d) surface microstructure of the AlN porous ceramic skeleton; (e) XRD; (f) compressive stress of the $P_I$, $P_{II}$, $P_{III}$, and $P_{IV}$.

After LSI (Fig. 3), the length, width and height of the ceramic skeletons were reduced to 10-20% of the porous green body skeleton. As the ceramic slurry solid loading was relatively low (33.33 wt.%), the organic resin in the porous green body was converted to carbon (C) after carbonization. If the solid loading is increased, the UV penetration is hindered and the skeleton cannot be printed. The surface of the skeletons exhibited more pores after LSI, and the size of the micropores was in the range of 1-10 μm [Fig. 3(b-d)]. The main phase of the porous ceramic skeleton after LSI was characterized by XRD, and the main phases were the AlN, Si and SiC [Fig. 3(e)]. The skeletons contained residual silica fume after LSI, which reacted with C in the carbonized skeleton to form SiC at 1550 ℃. The maximum compressive stress of the $P_I$, $P_{II}$, $P_{III}$, and $P_{IV}$ were 0.11, 0.45, 0.54, and 1.40 MPa, respectively [Fig. 3(f)]. The porosity of the ceramic skeletons was measured using the drainage method (Table 3),

and the uncertainty analysis of the porosity testing was conducted in the supplementary material.

**Table 3.** Porosity of the AlN porous ceramic skeletons.

| | $P_I$ | $P_{II}$ | $P_{III}$ | $P_{IV}$ |
|---|---|---|---|---|
| Porosity (%) | 82.20±0.46 | 75.24±0.39 | 74.16±0.39 | 60.46±0.39 |

### 3.2 Heat transfer analysis

The temperature change at $Q_1$, $Q_2$, and $Q_3$ were measured when the pure solar salt melted [Fig. 4(a)]. The temperature at $Q_1$ rapidly increased as the heat transfer time increased from 0-50 min, but the heating rate gradually decreased. At the initial stage of heat transfer, the pure solar salt near the heating wall accumulated a large amount of heat, and the heat storage technology mainly focuses on sensible heat storage. The temperature difference between $Q_1$ and $Q_2$ was up to 84.5 ℃. As the temperature increased and the heat transfer time exceeded 50 min, the solar salt near the heating wall began melting and entered the phase change heat storage stage. The heat transfer at this point occurred only through conduction [49, 50]. The temperatures at $Q_2$ and $Q_3$ also increased gradually with the increasing heat transfer time. Compared to $Q_1$, the heating rates at $Q_2$ and $Q_3$ were reduced. As the liquid fraction increased, the molten solar salt started moving toward the bottom wall due to gravity [51, 52]. The heat transfer mode changed from only conduction to a combination of conduction and convection, thereby enhancing the PCMs melting rate and accelerating the melting front expansion. The temperature difference between $Q_2$ and $Q_3$ was significantly reduced compared to that between $Q_1$ and $Q_2$. Once the heat transfer time exceeded 160 min,

the temperatures at $Q_1$, $Q_2$, and $Q_3$ gradually increased. As the temperature difference between these points and the heating plate was 300 ℃, the heat storage technology of the PCMs was classified as sensible heat storage. The temperature profile exhibited a linearly increasing trend for $Q_1$, $Q_2$, and $Q_3$ during the melting of the solar salt/$P_{I/IV}$ composite PCMs [Fig. 4(b, c)].

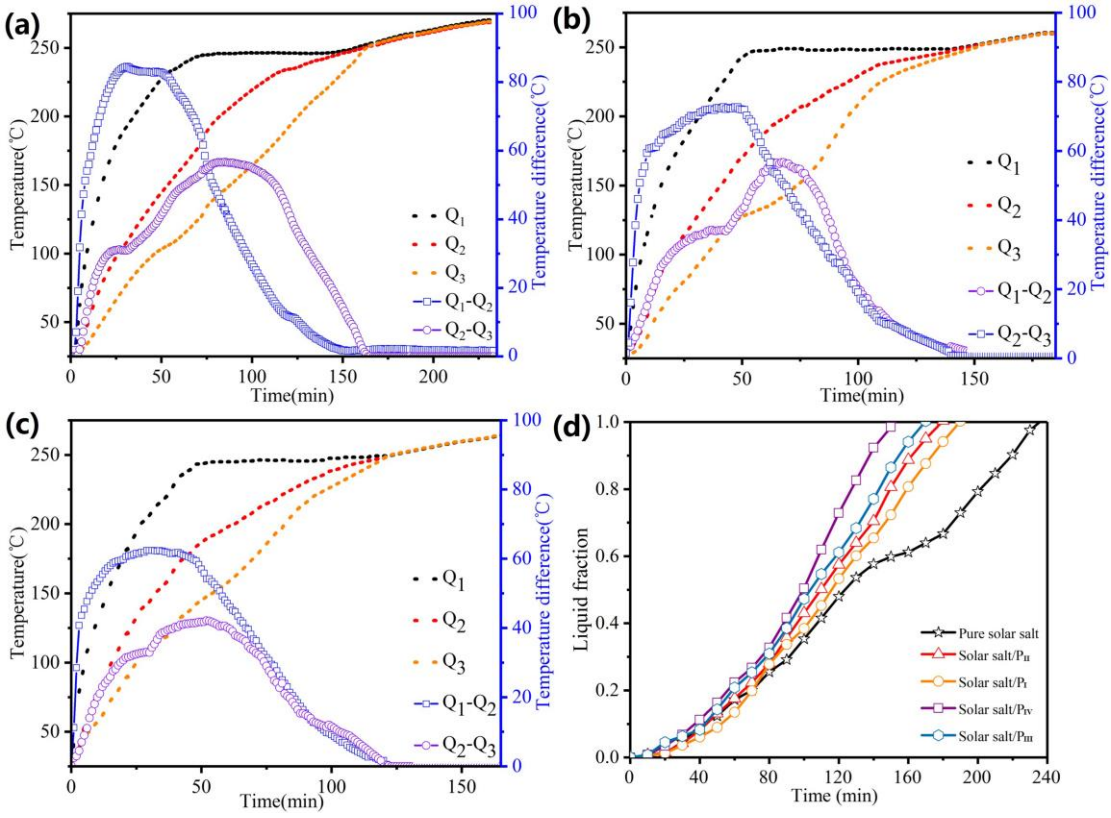


**Fig. 4.** Heat transfer test; (a) pure solar salt; (b) solar salt/$P_I$ composite PCMs; (c) solar salt/$P_{IV}$ composite PCMs; and (d) liquid fraction.

When the solar salt/ $P_{I/IV}$ composite PCMs melt, the temperature difference $Q_1$-$Q_2$ was 72.5 ℃ and 62.4 ℃, respectively, and that $Q_2$-$Q_3$ was 56.7 ℃ and 42.1 ℃. Compared to the pure solar salt, the temperature difference $Q_1$-$Q_2$ and $Q_2$-$Q_3$ were lower by 22.1 ℃ and 14.6 ℃, respectively, when the solar salt/$P_{IV}$ composite PCMs melt. As the heat conductivity of the ceramic skeleton was greater than that of the pure solar salt, the heat

transfer rate of the solar salt/AlN porous ceramic skeleton composite PCMs also increased comparatively.

**Table 4.** The melting time.

| | Solar salt | Solar salt/ $P_I$ composite PCMs | Solar salt/ $P_{II}$ composite PCMs | Solar salt/ $P_{III}$ composite PCMs | Solar salt/$P_{IV}$ composite PCMs |
|---|---|---|---|---|---|
| Time (min) | 233±2 | 185±2 | 175±1 | 172±2 | 156±2 |

The melted area was calculated using the ImageJ software, which can accurately identify and measure the pixel-based solid and liquid areas of the PCMs. The melted volume fraction refers to the ratio of the liquid areas occupying the front wall surface areas of the quartz cuboid box. The PCMs liquid fraction gradually increased at the initial melting stage (melting time<40 min) as the heat transfer occurred mainly through conduction [Fig. 4(d)]. Subsequently, with the increasing liquid fraction, the PCMs heat transfer became a combination of convection and conduction, further increasing the liquid fraction rapidly. However, with the suppression of convection over time, the liquid fraction decreased towards the end of the melting stage.

The melting time of the pure solar salt was 233±2 min (Table 4), whereas that of the $P_I$, $P_{II}$, $P_{III}$, and $P_{IV}$ composite PCMs was 185±2, 175±1, 172±2, and 156±2 min, respectively. The melting time of the composite PCMs was lower than that of the pure salt (by up to 33.05%), increasing with the porosity of the ceramic skeleton. Although the increased porosity inhibited the PCMs heat convection, the improvement in thermal conductivity far outweighed these effects.

The ceramic skeletons were prepared by the sol-gel, direct foaming, gel injection, and organic porous impregnation methods to enhance the PCMs heat storage rate [53]. These ceramic skeletons, however, exhibited uncontrollable structures and non-uniform pore sizes. The pore size, strut dimensions, and complex structures could be controlled by using the photocuring 3D printing technology. This complex porous ceramic skeleton is anticipated to be used in future heat storage devices with complex structures and widely applied in the field of medium- and high-temperature PCMs thermal storage, making up for their inadequate corrosion resistance in metal porous foam structures. However, compared to the ceramic skeletons prepared using other methods [36, 45, 54, 55], the AlN porous ceramic skeleton prepared in this study exhibited lower solid loading and thermal conductivity.

The heat transfer in nonmetallic materials mainly relies on lattice vibrations [56]. Solar salts exhibit serious lattice defects; the phonons present within them are scattered during heat transfer [57, 58]. However, the AlN porous ceramic skeleton improves the mean free path of the phonons and attenuates phonon scattering [55]. The experiments showed that the thermal conductivities of the $P_I$, $P_{II}$, $P_{III}$, and $P_{IV}$ composite PCMs were 1.05, 1.31, 1.33, and 1.46 W/(m·K), respectively. Compared to the pure solar salt (0.59 W/(m·K)) [59], the thermal conductivity of the composite PCMs increased by 77.97%, 122.03%, 125.44%, and 147.46%, respectively.

Fig. 5 shows the temperature gradients of the pure solar salt and the composite PCMs after melting for 40, 80, 120, and 160 min. Initially, the heat was primarily transferred through conduction, and the melting front was almost parallel to the heating

wall [Fig. 5(a1)]. However, with the increasing liquid fraction, the melting front gradually tilted and took the shape of a large circular triangle. As the temperature of the solar salt decreased, it flowed along the solid-liquid boundary toward the bottom wall. Moreover, due to the heat convection, the temperature difference between the solid and liquid phases was lower at the bottom wall, slowing down the melting rate [60,61] and resulting in an inverted melted salt triangle at the bottom wall [Fig. 5(a2)]. The melting front moved downward as the solar salt continued to melt, and the shape of the unmelted solar salt gradually changed from a trapezoid to a triangle until it completely melted [Figs. 5(a3, a4)]. Moreover, the melted liquid fraction of the composite PCMs was greater than that of the pure solar salt, decreasing with the increasing porosity of the AlN porous ceramic skeleton [Figs. 5(b-e)].

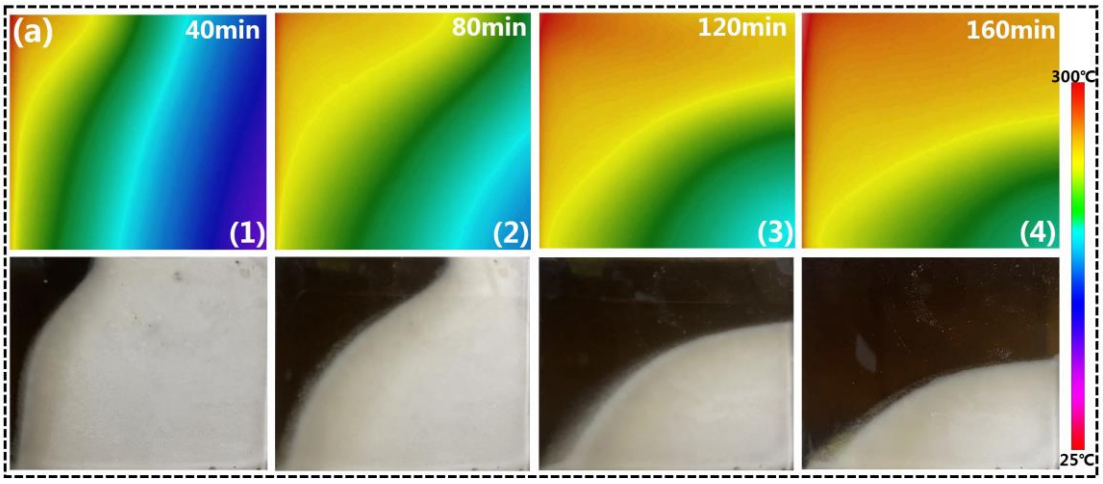

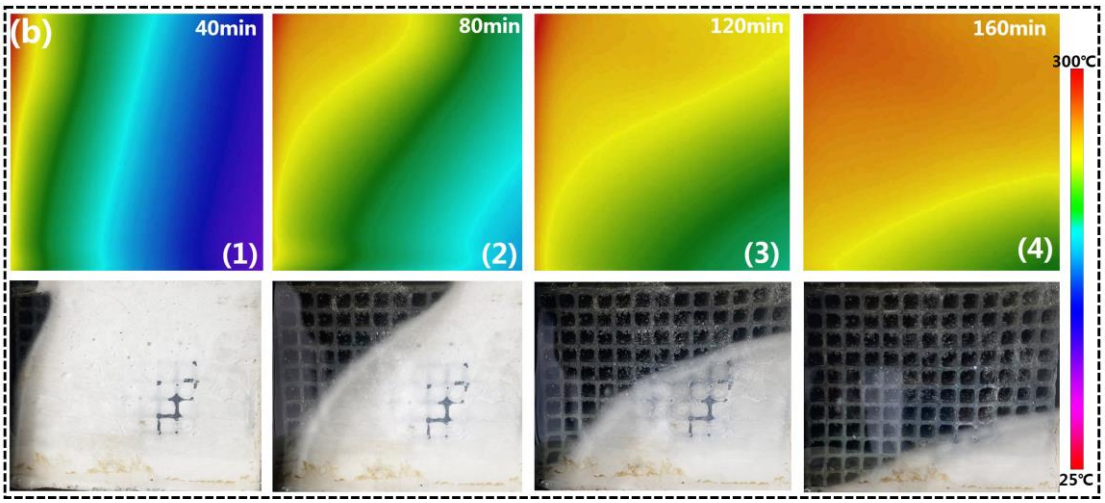
(b)
40min
80min
120min
160min
(1)
(2)
(3)
(4)
300℃
25℃

1

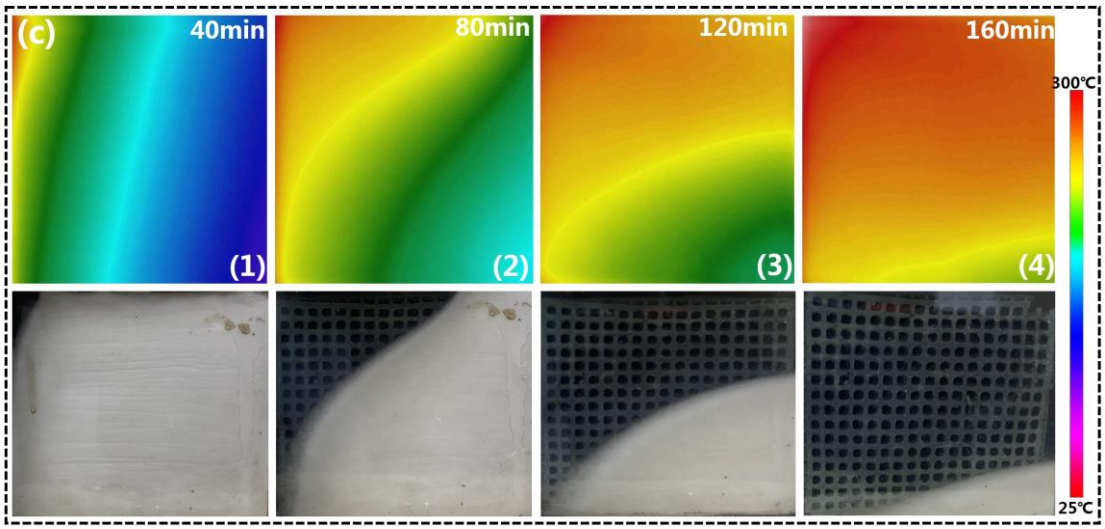
(c)
40min
80min
120min
160min
(1)
(2)
(3)
(4)
300℃
25℃

2

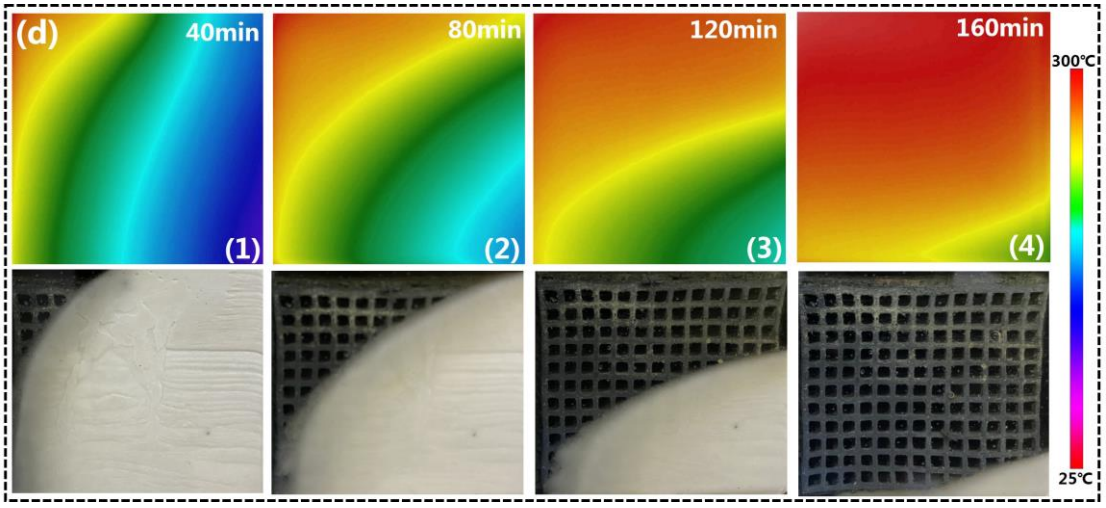
(d)
40min
80min
120min
160min
(1)
(2)
(3)
(4)
300℃
25℃

3

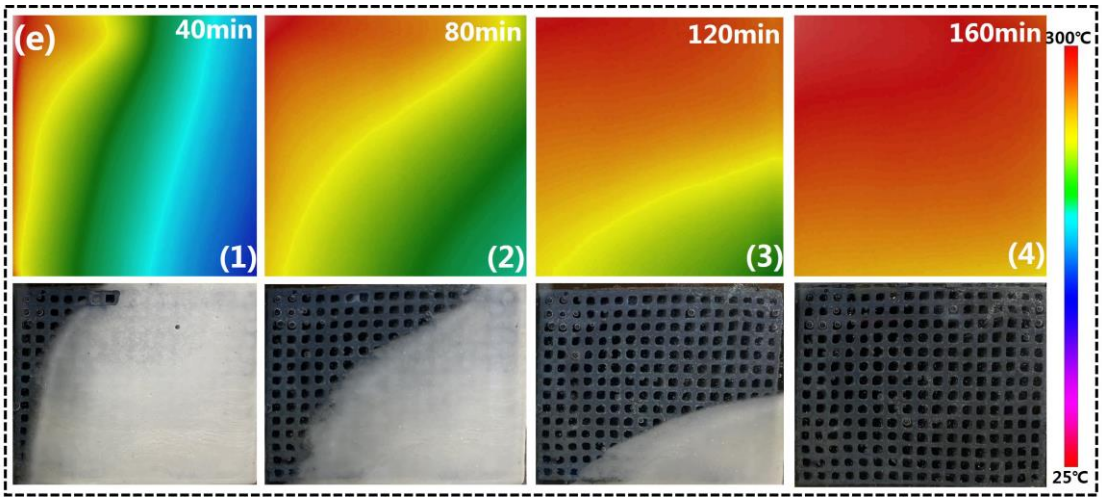


**Fig. 5.** PCMs temperature field during melting; (a) pure solar salt; and (b–e) solar salt/$P_{I, II, III, and IV}$ composite PCMs, respectively.

## 3.3 Anti-corrosion analysis

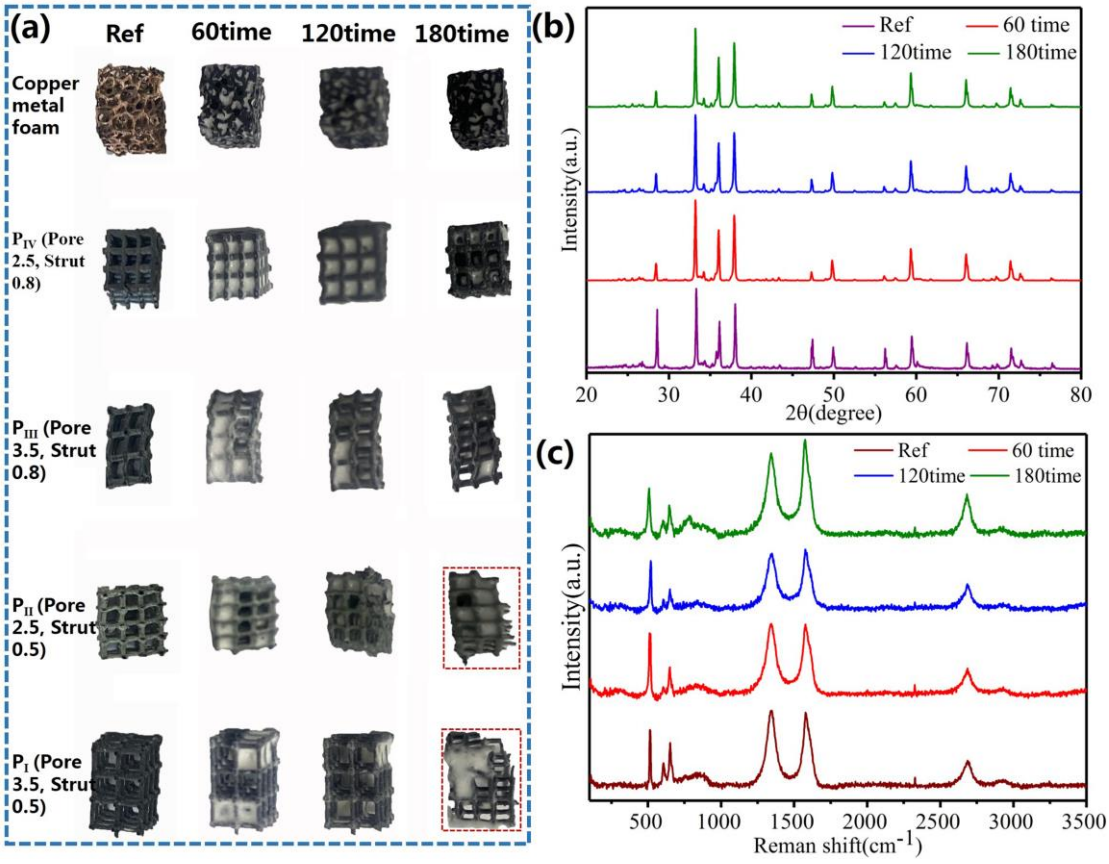


**Fig. 6.** Corrosion test results: (a) AlN porous ceramic skeleton after the heat cycles; and (b and c) XRD and Raman spectrum of the AlN porous ceramic skeleton after the heat cycles, respectively.

Fig. 6(a) shows the AlN porous ceramic skeleton and Cu foam after the heat cycle tests. The Cu foam surface color changed from yellow to black after 60 heat cycles due to corrosion by $NaNO_3$ and $KNO_3$, reducing its heat conductivity and service life [62,63]. After 180 heat cycles, the $P_I$ and $P_{II}$ composites cracked, whereas $P_{III}$ and $P_{IV}$ did not. Due to its thermal expansion during the phase transition, the solar salt interacts with the ceramic skeleton. The maximum compressive stress of $P_{III}$ and $P_{IV}$ is greater than that of $P_I$ and $P_{II}$ (Fig. 3(f)). The phase and functional groups of the ceramic skeleton, after the heat cycles, were analyzed by XRD and Raman spectroscopy [Figs. 6(b, c)]. The composition of the AlN porous ceramic skeleton remained unchanged and no new substances were formed, as revealed by the sharp XRD peaks. This indicated that the ceramic skeleton did not corrode.

In addition, the elemental content analysis of the ceramic skeleton by energy dispersive spectroscopy (EDS) revealed the major elements to be Al, N, and C [Figs. 7(a-d), along with sodium (Na), oxygen (O), potassium (K), and Si [Figs. S2-4].

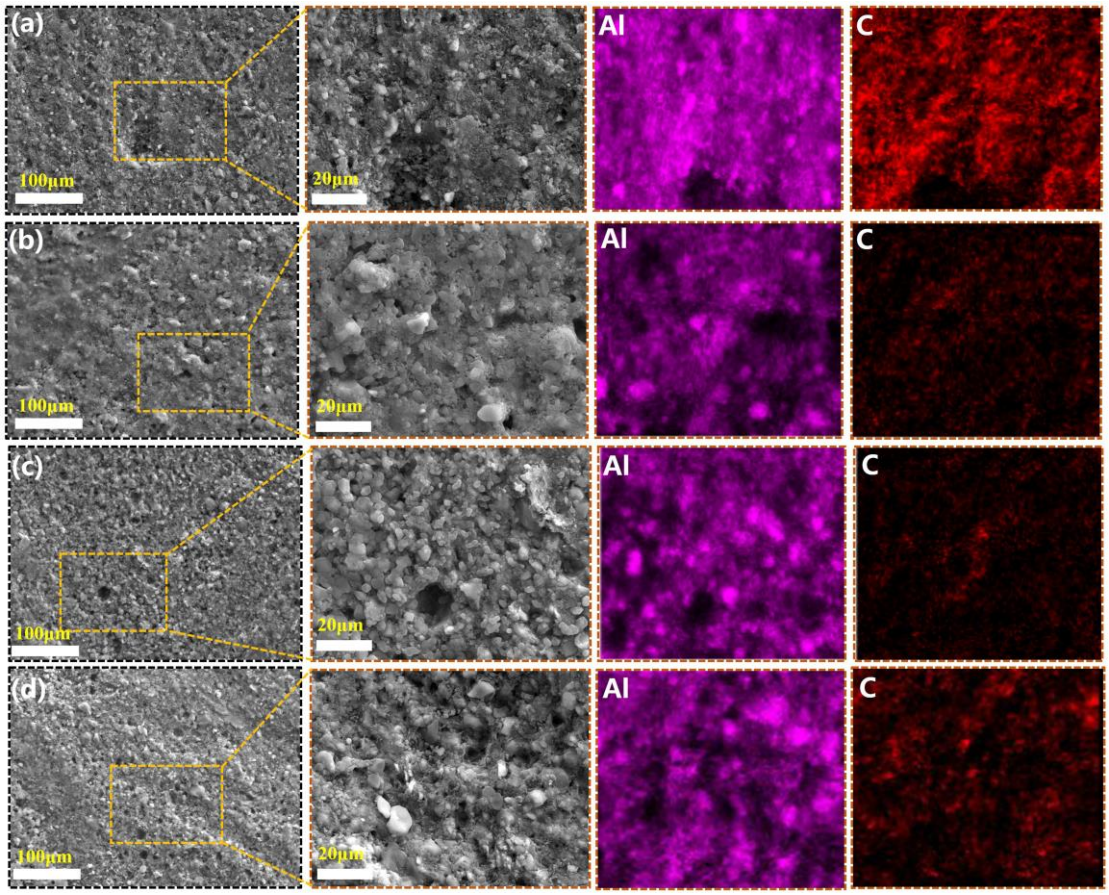


**Fig. 7.** EDS analysis (a) Ref; and after (b–d) 60, 120, and 180 heat cycles for the AlN porous ceramic skeleton.

## 4. Conclusion

In this study, the AlN porous ceramic skeletons with controllable structures were prepared using an LCD 3D printer. The solar salt/AlN porous ceramic skeleton composite PCMs was fabricated through the impregnation of solar salt into AlN porous ceramic skeleton. It effectively shortens the melting time of solar salt and reduces the temperature difference in the internal temperature field during the melting process. Additionally, the ceramic skeleton exhibits excellent anti-corrosion against solar salt. The main conclusions of this study are presented as follows:

(1) The porosities of the $P_I$, $P_{II}$, $P_{III}$, and $P_{IV}$ is 82.21%, 75.21%, 74.23%, and 60.15%,

respectively, and their maximum compressive stresses are 0.11, 0.45, 0.54, and 1.40 MPa, respectively.

(2) When solar salt/$P_{IV}$ composite phase change materials melts, the temperature difference between $Q_1$-$Q_2$ and $Q_2$-$Q_3$ is 62.4 ℃ and 42.1 ℃, respectively, lower than those for the pure solar salt by 22.1 ℃ and 14.6 ℃, respectively.

(3) The melting time of pure solar salt is 233±2 min, whereas that of the solar salt /$P_I$, $P_{II}$, $P_{III}$, and $P_{IV}$ composite phase change materials are 185±2, 175±1, 172±2, and 156±2 min, respectively.

(4) The melting time of the composite phase change materials increases with the increasing porosity of the aluminum nitride porous ceramic skeleton. The maximum melting rate of the composite phase change materials increases by 33.05% compared to that of the pure solar salt.

(5) After 180 heat cycles, the Cu foam is corroded by the solar salt, and the $P_I$ and $P_{II}$ skeletons cracks. However, *X*-ray diffraction and Raman spectra analysis show that the compositions of the skeletons do not change and no new substances are produced.

(6) The solar salt impregnates the ceramic skeleton through the surface pores. The energy dispersive spectroscopy results show that the ceramic skeleton contains Al, N, and C, in addition to Na, K, and O, even after 180 heat cycles.

**Credit author statement**

**Huan Wang:** Writing-review & editing, Writing-original draft, Methodology, Investigation. **Ziyuan Li:** Investigation. **Zhen Shang:** Writing-original draft,

Investigation. **Limei Tian:** Supervision, Funding acquisition, Writing-review & editing. **Shuai Zhang:** Investigation. **Yuying Yan:** Methodology.

## Declaration of competing interest

The authors declare that they have no known competing financial interests or personal relationships that could have appeared to influence the work reported in this paper.

## Data availability

Data will be made available on request.

## Acknowledgements

The authors are grateful for grants received from the National Key R&D Program of China (No. 2018YFA0702300), the Program for JLU Science and Technology Innovative Research Team (No. 2020TD-03).

## Reference

[1] Z. Khan, Z. Khan, A. Ghafoor, A review of performance enhancement of PCM based latent heat storage system within the context of materials, thermal stability and compatibility, Energ. Convers. Manage. 115 (2016) 132-158.

[2] S. Zhang, D. L. Feng, L. Shi, L. Wang, Y. G. Jin, L. M. Tian, Z. Y. Li, G. Y. Wang, L. Zhao, Y. Y. Yan, A review of phase change heat transfer in shape-stabilized phase change materials (ss-PCMs) based on porous supports for thermal energy storage, Renew. Sust. Energ. Rev. 135 (2020) 110127.

[3] Fitriani, R. Ovik, B. D. Long, M. C. Barma, M. Riaz, M. F. M. Sabri, S. M. Said, R. Saidur, A review on nanostructures of high-temperature thermoelectric materials for waste heat recovery, Renew. Sust. Energ. Rev. 64 (2016) 635-659.

[4] M. Esen, T. Ayhan, Development of a model compatible with solar assisted cylindrical energy storage tank and variation of stored energy with time for different phase change materials, Energ. Convers. Manage. 37(12) (1996) 1775-1785.

[5] M. Esen, A. Durmus, A. Durmus, Geometric design of solar-aided latent heat store depending on various parameters and phase change materials, Sol. Energy 62(1) (1998) 19-28.

[6] M. Esen, Thermal performance of a solar-aided latent heat store used for space heating by heat pump, Sol. Energy 69(1) (2000) 15-25.

[7] M. J. Mochane, T. C. Mokhena, T. E. Motaung, L. Z. Linganiso, Shape-stabilized phase change materials of polyolefin/wax blends and their composites A systematic review, J. Therm. Anal. Calorim. 139(5) (2020) 2951-2963.

[8] H. Nazir, M. Batool, F. J. B. Osorio, M. Isaza-Ruiz, X. H. Xu, K. Vignarooban, P. Phelan, Inamuddin, A. M. Kannan, Recent developments in phase change materials for energy storage applications: A review, Int. J. Heat Mass. Tran. 129 (2019) 491-523.

[9] A. Pignata, F. D. Minuto, A. Lanzini, D. Papurello, A feasibility study of a tube bundle exchanger with phase change materials: A case study, J. Build. Eng. 78 (2023) 107622.

[10] H. Ben Bacha, A. S. Abdullah, A. Kabeel, M. Abdelgaied, Design and development of a tubular solar distiller using a convex absorber, wick materials, and PCM reservoir combined with a solar parabolic concentrator, J. Energy Storage 62 (2023) 106897.

[11] N. Soares, T. Matias, L. Duraes, P.N. Simoes, J. J. Costa, Thermophysical characterization of paraffn-based PCMs for low temperature thermal energy storage applications for buildings, Energy 269 (2023) 126745.

[12] T. Mhedheb, W. Hassen, A. Mhimid, M. A. Almeshaal, M. Alhadri, L. Kolsi, Parametric

analysis of a solar parabolic trough collector integrated with hybrid-nano PCM storage tank, Case Stud. Therm. Eng. 51 (2023) 103652.

[13] Y. X. Lin, G. Alva, G. Y. Fang, Review on thermal performances and applications of thermal energy storage systems with inorganic phase change materials, Energy 165(A) (2018) 685-708.

[14] A. Al-Ahmed, A. Sari, M. A. J. Mazumder, B. Salhi, G. Hekimoglu, F. A. Al-Sulaiman, Inamuddin, Thermal energy storage and thermal conductivity properties of fatty acid/fatty acid-grafted-CNTs and fatty acid/CNTs as novel composite phase change materials, Sci Rep-UK. 10(1) (2020) 15388.

[15] K. Kant, P. H. Biwole, I. Shamseddine, G. Tlaiji, F. Pennec, F. Fardoun, Recent advances in thermophysical properties enhancement of phase change materials for thermal energy storage, Sol. Energ. Mat. Sol. C. 231 (2021) 111309.

[16] A. Zaib, A. R. Mazhar, T. Talha, M. Inshal, Experimental investigation of a solar PCM heat exchanger for indoor temperature stabilization, Energ Buildings 297 (2023) 113478.

[17] A. Marra, M. Santarelli, D. Papurello, Solar Dish Concentrator: A Case Study at the Energy Center Rooftop, Int. J. Energ. Res. 2023 (2023) 9658091.

[18] Y. Tian, X. Liu, H. B. Zheng, Q. Xu, Z. Zhu, Q. Luo, C. Song, K. Gao, C. Dang, Y. Xuan, Artificial mitochondrion for fast latent heat storage: Experimental study and lattice Boltzmann simulation, Energy 245 (2022) 123296.

[19] Z. Q. Zhu, M. J. Liu, N. Hu, Y. K. Huang, L. W. Fan, Z. T. Yu, J. Ge, Inward Solidification Heat Transfer of Nano-Enhanced Phase Change Materials in a Spherical Capsule: An Experimental Study, J. Heat Trans-T. Asm. 140(2) (2018) 022301.

[20] R. Cozzolino, D. Chiappini, G. Bella, Experimental characterization of a novel thermal energy

storage based on open-cell copper foams immersed in organic phase change material, Energ. Convers. Manage. 200 (2019) 112101.

[21] A. Alhusseny, N. Al-Zurfi, A. Nasser, A. Al-Fatlawi, M. Aljanabi, Impact of using a PCM-metal foam composite on charging/discharging process of bundle d-tub e LHTES units, Int. J. Heat Mass Tran. 150 (2020) 119320.

[22] Y. H. Diao, L. Liang, Y. H. Zhao, Z. Y. Wang, F. W. Bai, Numerical investigation of the thermal performance enhancement of latent heat thermal energy storage using longitudinal rectangular fins and flat micro-heat pipe arrays, Appl. Energy 233 (2019) 894-905.

[23] N. S. Bondareva, B. Buonomo, O. Manca, M. A. Sheremet, Heat transfer performance of the finned nano-enhanced phase change material system under the inclination influence, Int. J. Heat. Mass Tran. 135 (2019) 1063-1072.

[24] J. L. Tao, J. D. Luan, Y. Liu, D. Y. Qu, Z. Yan, X. Ke, Technology development and application prospects of organic-based phase change materials: An overview, Renew. Sust. Energ. Rev. 159 (2022) 112175.

[25] S. Bell, T. Steinberg, G. Will, Corrosion mechanisms in molten salt thermal energy storage for concentrating solar powerm, Renew. Sust. Energ. Rev. 114 (2019) 109328.

[26] A. Sole, L. Miro, C. Barreneche, I. Martorell, L. F. Cabeza, Corrosion f metals and salt hydrates used for thermochemical energy storage, Renew. Energ. 75 (2015) 519-523.

[27] Z. P. Li, Z. W. Huang, N. Xie, X. N. Gao, Y. T. Fang, Z. G. Zhang, Preparation of $Al_2O_3$-coated expanded graphite with enhanced hydrophilicity and oxidation resistance, Ceram. Int. 44(14) (2018) 16256-16264.

[28] M. K. Saranprabhu, D. Chandini, P. Bharathidasan, S. Devaraj, K. S. Rajan, Lowered total

solidification time and increased discharge rate of reduced graphene oxide-solar salt composites: Potential for deployment in latent heat thermal energy storage system, Sol. Energy 204 (2020) 466-475.

[29] S. Harish, D. Orejon, Y. Takata, M. Kohno, Enhanced thermal conductivity of phase change nanocomposite in solid and liquid state with various carbon nano inclusions, Appl. Therm. Eng. 114 (2017) 1240-1246.

[30] B. Kalidasan, A. K. Pandey, R. Saidur, M. Samykano, V. V. Tyagi, Nano additive enhanced salt hydrate phase change materials for thermal energy storage, Int. Mater. Rev. 68(2) (2022) 140-183.

[31] G. D. Wehinger, S. T. Kolaczkowski, L. Schmalhorst, D. Beton, L. Torkuhl, Modeling fixed-bed reactors from metal-foam pellets with detailed CFD, Chem. Eng. J. 373 (2019) 709-719.

[32] F. Xue, Y. Lu, X. D. Qi, J. H. Yang, Y. Wang,Melamine foam-templated graphene nanoplatelet framework toward phase change materials with multiple energy conversion abilities, Chem. Eng. J. 365 (2019) 20-29.

[33] J. X. Ma, S. H. Zheng, F. Zhou, Y. Y. Zhu, P. Das, R. Huang, L. Z. Zhang, X. Wang, H. Wang, Y. Cui, Z. S. Wu, All 3D printing lithium metal batteries with hierarchically and conductively porous skeleton for ultrahigh areal energy density, Energy Storage Mater. 54 (2022) 304-312.

[34] J. Ouyang, X. M. Wang, L. C. Wang, W. N. Xiong, M. Y. Li, Z. H. Hua, L. L. Zhao, C. Zhou, X. B. Liu, H. Chen, Y. F. Luo, Construction of a porous carbon skeleton in wood tracheids to enhance charge storage for high-performance supercapacitors, Carbon, 196 (2022) 532-539.

[35] H. Wang, Z. Y. Li, Z. Shang, L. M. Tian, Preparation of porous SiC ceramics skeleton with low-cost and controllable gradient based on liquid crystal display 3D printing, J. Eur. Ceram.

Soc. 42 (2022) 5432-5437.

[36] H. R. Wang, X. F. Ran, Y. J. Zhong, L. Y. Lu, J. Lin, G. He, L. Wang, Z. M. Dai, Ternary chloride salteporous ceramic composite as a high temperature phase change material, Energy 238(B) (2022) 121838.

[37] T. Ohji, M. Fukushima, Macro-porous ceramics: processing and properties. Int. Mater. Rev. 57(2) (2012) 115-131.

[38] X. B. Huang, X. Chen, A. Li, D. Atinafu, H. Y. Gao, W. J. Dong, G. Wang, Shape-stabilized phase change materials based on porous supports for thermal energy storage applications, Chem. Eng. J. 356 (2019) 641-661.

[39] Q. Y. Luo, X. L. Liu, H. L. Wang, Q. Xu, Y. Tian, T. Liang, Q. Liu, Z. Liu, X. H. Yang, Y. M. Xuan, Y. L. Li, Y. L. Ding, Synergetic enhancement of heat storage density and heat transport ability of phase change materials inlaid in 3D hierarchical ceramics, Appl. Energy 306 (2021) 117995.

[40] C. Li, Q. Li, Y. L. Ding, Investigation on the effective thermal conductivity of carbonate salt based composite phase change materials for medium and high temperature thermal energy storage, Energy 176 (2019) 728-741.

[41] Q. Xu, X. L. Liu, Q. Y. Luo, Y. Tian, C. Z. Dang, H. C. Yao, C. Song, Y. M. Xuan, J. M. Zhao, Y. L. Ding, Loofah-derived eco-friendly SiC ceramics for high-performance sunlight capture, thermal transport, and energy storage, Energy Storage Mater. 45 (2022) 786-795.

[42] S. Zhang, Z. Y. Li, Y. P. Yao, L. M. Tian, Y. Y. Yan, Heat transfer characteristics and compatibility of molten salt/ceramic porous composite phase change material, Nano energy. 100 (2022) 107476.

[43] C. Heisel, C. Caliot, T. Chartier, S. Chupin, P. David, D. Rochais, Digital design and 3D printing of innovative SiC architectures for high temperature volumetric solar receivers, Sol. Energ. Mat. Sol. C. 232 (2021) 111336.

[44] M. Pelanconi, M. Barbato, S. Zavattoni, G.L. Vignoles, A. Ortona, Thermal design, optimization and additive manufacturing of ceramic regular structures to maximize the radiative heat transfer, Mater. Design 163 (2019) 107539.

[45] F. Yang, G. L. Zhao, C. Zhou, D. Lin, Phase change materials (PCM) based cold source for selective freezing 3D printing of porous materials, Int. J. Adv. Manuf. Technol. 95 (2018) 2145-2155.

[46]C. Villada, A. Bonk, T. Bauer, F. Bolivar, High-temperature stability of nitrate/nitrite molten salt mixtures under different atmospheres, Appl. Energ. 226 (2018) 107-115.

[47] X. Hu, F. Zhu, X. Gong, Experimental and numerical study on the thermal behavior of phase change material infiltrated in low porosity metal foam, J. Energy Storage 26 (2019) 101005.

[48] Z. Zhang, J. Cheng, X. He, Numerical simulation of flow and heat transfer in composite PCM on the basis of two different models of open-cell metal foam skeletons, Int. J. Heat Mass Tran. 112 (2017) 959-971.

[49] D. Feng, J. Nan, Y. Feng, X. Zhang, Y. Yan, Numerical investigation on improving the heat storage and transfer performance of ceramic/D-mannitol composite phase change materials by bionic graded pores and nanoparticle additives, Int. J. Heat Mass Tran. 179 (2021) 121748.

[50] P. Zhang, Z. Meng, H. Zhu, Y. Wang, S. Peng, Melting heat transfer characteristics of a composite phase change material fabricated by paraffin and metal foam, Appl. Energy 185(SI 2) (2017) 1971-1983.

[51] A. Saraswat, R. Bhattacharjee, A. Verma, M. Das, S. Khandekar, Investigation of diffusional transport of heat and its enhancement in phase-change thermal energy storage systems, Appl. Therm. Eng. 111 (2017) 1611-1621.

[52] Q. Han, H. Wang, C. Yu, C. Zhang, Lattice Boltzmann simulation of melting heat transfer in a composite phase change material, Appl. Therm. Eng. 176 (2020) 115423.

[53] Y. H. Chen, J. X. Sun, P. Y. Jiang, Z. H. Chai, B. Q. Zhang, J. H. Li, Review on Porous Ceramic-Based Form-Stable Phase Change Materials: Preparation, Enhance Thermal Conductivity, and Application, Chembioeng Rev. 10 (2023) 1-19.

[54] Z. Y. Wang, S. X. Zhu, X. Y. Zhao, L. Huang, D. Q. Zou, Preparation and thermal performance of a novel alloy microencapsulated phase change material (MEPCM)/ceramic composite, Int. J. Therm. Sci. 176 (2022) 107478.

[55] L. Qiu, K. N. Yan, Y. H. Feng, X. L. Liu, X. X. Zhang, Bionic hierarchical porous aluminum nitride ceramic composite phase change material with excellent heat transfer and storage performance, Compos. Commun. 27 (2021) 100892.

[56] K. J. Yuan, J. M. Shi, W. Aftab, M. L. Qin, A. Usman, F. Zhou, Y. Lv, S. Gao, R. Q. Zou, Engineering the Thermal Conductivity of Functional Phase-Change Materials for Heat Energy Conversion, Storage, and Utilization, Adv. Funct. Mater. 30(8 SI) (2020) 1904228.

[57] G. C. Q. Pan, J. Ding, P. Chen, H. Yan, Y. F. Du, D. J. Lee, Y. T. Lu, Finite-size effects on thermal property predictions of molten salts, Sol. Energ. Mat. Sol. C. 54 (2021) 105294.

[58] H. X. Lyu, D. L. Feng, Y. H. Feng, X. X. Zhang, Enhanced thermal energy storage of sodium nitrate by graphene nanosheets: Experimental study and mechanisms, J. Energy Storage. 54 (2022) 1052940.

[59] S. Zhang, Y. Yan, Energy, exergy and economic analysis of ceramic foam-enhanced molten salt as phase change material for medium-and high-temperature thermal energy storage, Energy 262(A) (2022) 125462.

[60] Y. Yao, H. Wu, Pore-scale simulation of melting process of paraffin with volume change in high porosity open-cell metal foam, Int. J. Therm. Sci. 138 (2019) 322-340.

[61] V. Joshi, M. Rathod, Thermal performance augmentation of metal foam infused phase change material using a partial filling strategy: An evaluation for fill height ratio and porosity, Appl. Energy. 253 (2019) 113621.

[62] S. Fernandez, M. Alvarez, Passivity breakdown and stress corrosion cracking of alpha-brass in sodium nitrate solutions, Corros. Sci. 53(1) (2011) 82-88.

[63] M. Scendo, Inhibition of copper corrosion in sodium nitrate solutions with nontoxic inhibitors, Corros. Sci. 50(6) (2008) 1584-1592.